Supporting Information

Jahanshad et al. 10.1073/pnas.1216206110

SI Text

Establishing Zygosity and Genotyping. Here, we analyzed a high-angular resolution diffusion imaging (HARDI) -imaged subsample of a much larger genotyped twin population. Subjects were screened to exclude cases of pathology known to affect brain structure. No subjects reported a history of significant head injury, neurological or psychiatric illness, or substance abuse or dependence, and no subjects had a first-degree relative with a psychiatric disorder. All subjects were right-handed as determined using 12 items from Annett's Handedness Questionnaire (1). Zygosity was initially established objectively by typing nine independent DNA microsatellite polymorphisms (polymorphism information content > 0.7) using standard PCR methods and genotyping. Results were cross-checked with blood group (ABO, MNS, and Rh) and phenotypic data (hair, skin, and eye color), giving an overall probability of correct zygosity assignment > 99.99%. Subsequently zygosity was confirmed by genome-wide association scan (GWAS). Genomic DNA samples were analyzed on the Human610-Quad BeadChip (Illumina) according to the manufacturer's protocols (Infinium HD Assay). Quality control procedures on the zygosity and familial relatedness of individuals within the cohort have previously been established. Families with ancestry deviating from the European population were determined as in ref. 2. Briefly, non-Australian European populations were used to calculate mean reference first and second principle component scores (PC1 and PC2). Any Australian individual more than 6 SDs from this mean for either PC1 or PC2 was deemed to be an ancestry outlier and removed from the GWAS analyses. Additionally, the pedigree structures for this study were examined and confirmed using Graphic Representation of Relationships (3).

Imaging Parameters. T1-weighted images were acquired with an inversion recovery rapid gradient echo sequence. Acquisition parameters were: inversion/repetition/echo time (TI/TR/TE) = 700/1500/3.35 ms; flip angle = 8 degrees; slice thickness = 0.9mm, with an acquisition matrix of 256 × 256. Diffusion-weighted images (DWI) were acquired using single-shot echo planar imaging (EPI) with a twice-refocused spin echo sequence to reduce eddy-current induced distortions. Acquisition parameters were optimized to improve the signal-to-noise ratio for estimating diffusion tensors (4). Imaging parameters were: 23 cm FOV, TR/TE 6090/91.7 ms, with a 128 × 128 acquisition matrix. Each 3D volume consisted of 55 2-mm thick axial slices with no gap and a 1.79 × 1.79 mm^2 in-plane resolution. 105 images were acquired per subject: 11 with no diffusion sensitization (i.e., T2-weighted b_0 images) and 94 DWI (b = 1159 s/mm^2) with gradient directions distributed on the hemisphere. Scan time was 14.2 minutes.

Heritability Analysis of Connectivity.

$$Z = Aa + Cc + Ee : \qquad \textbf{[S1]}$$

in Eq. **S1**, Z can be any quantitative phenotypic trait—in this case, the fiber count proportion at a particular matrix element. A, C, and E are latent (unobserved) variables, and a, c, and e are the weights of each parameter determined by optimizing Σ by full information maximum likelihood estimation. The variance components combine to create the total observed interindividual variance, and therefore, Eq. **S2** is satisfied:

$$a^2 + c^2 + e^2 = 1. \qquad \textbf{[S2]}$$

This form of the structural equation model uses the full information maximum likelihood estimation (Eq. **S3**) with a χ^2-distributed null distribution to estimate genetic vs. environmental contributions to the observed variance, where m is the number of twin pairs in each group [49 for monozygotic (MZ) and 65 for dizygotic (DZ)], S_g is the observed covariance matrix for each twin group g, and Σ_g is the expected covariance matrix (Eq. **S4**) for group g, with $\alpha = 1$ for the MZ group and $\alpha = 0.5$ for DZ:

$$FIML_g = N_g\left\{\ln|S_g| - \ln|\Sigma_g| + tr\left(S_g\Sigma_g^{-1}\right) - 2m\right\} \qquad \textbf{[S3]}$$

and

$$\Sigma_g = \begin{bmatrix} a^2 + c^2 + e^2 & \alpha a^2 + c^2 \\ \alpha a^2 + c^2 & a^2 + c^2 + e^2 \end{bmatrix}. \qquad \textbf{[S4]}$$

In structural equation models, the χ^2 goodness of fit measure determines a P value for all specified regions of interest (elements of the matrix) where the test is performed. This value indicates that the model is a good fit to the data if $P > 0.05$ (this direction is the opposite of the usual convention that rejects models or hypotheses when $P < 0.05$). To determine the significance of a particular factor, specifically the A or C factor, the χ^2 goodness of fit values of the model may be compared with those values for a model that does not include that factor [i.e., to a shared environmental (C)/ unique environmental (E) model to determine the significance of the additional A factor; to an additive genetic (A) /E model to determine the significance of the C factor], giving Eq. **S5**:

$$p(A) = \chi^{2^{-1}}_{1DF}\left[\chi^2(ACE) - \chi^2(CE)\right], \qquad \textbf{[S5]}$$

where $\chi^{2^{-1}}_{1DF}$ denotes the inverse of the cumulative distribution function for a χ^2 distributed variable with one degree of freedom. Similar formulations apply for $p(C)$. In this case, low P values express significant improvements when adding a factor.

OpenMx software (openmx.psyc.virginia.edu/) (5) was implemented in the R statistical package (version 2.9.2; http://www.r-project.org/) to calculate the A/C/E parameters. The covariates—sex, age, and total intracranial volume (ICV)—were added to the model.

The genetic contributions to brain connections were estimated with a classical twin A/C/E structural equation model, including covariates. The A/C/E model did not fit the data better than the simpler A/E model. We, therefore, proceeded with the A/E model, which was a significantly better fit to the data than if all network variance was attributable to unique subject-specific effects.

Split Sample Replication. Groups were split according to study identification numbers uniquely assigned for each subject as they entered into the study. All family members were assigned to the same group. No significant differences were seen between the two groups in sex (P = 0.91) or ICV (as measured by the volume inside the skull-stripped T1-weighted images; P = 0.06). However, because the study was structured to contain a narrow range of ages corresponding to young adults between the ages of 21 and 30 y, there was a significant difference in age as calculated through a two-sided t test of the populations (P = 1.2×10^{-18}; mean group 1 = 24.4; mean group 2 = 22.6). This

difference was expected—because of the narrow age range of this study, older Australian twins approaching the age cutoff (30 y) were recruited into the study first to allow for maximal subject participation. Age, sex, and ICV were used as standard covariates in the genome-wide scan.

Full-Sample Connectome-Wide, Genome-Wide Scan. The two groups of healthy young adults were later combined to maximize the power for association. The most strongly associated SNPs within the same locus were found to reach connectome-wide, genome-wide significance as defined earlier. The Manhattan Plot of association statistics across the genome is shown in Fig. S3. Genome-wide significant results across the connections of the full sample are shown in Table S3. A full-scale quantile–quantile plot is shown in Fig. S4 combining all *P* values from all tested connections.

Tensor-Based Morphometry Study of the Alzheimer's Disease Neuroimaging Initiative Cohort. Briefly, the Alzheimer's Disease Neuroimaging Initiative (ADNI) is a large 5-y study launched in 2004 by the National Institute on Aging, the National Institute of Biomedical Imaging and Bioengineering, the Food and Drug Administration, private pharmaceutical companies, and nonprofit organizations. Subjects were recruited from 58 sites in the United States. The study was conducted according to the Good Clinical Practice guidelines, the Declaration of Helsinki, and US 21 CFR Parts 50 (Protection of Human Subjects) and 56 (Institutional Review Boards). Written informed consent was obtained from all participants before protocol-specific procedures were performed. All ADNI data are publicly available (http://www.loni.ucla.edu/ADNI/). To avoid effects of population stratification on genetic analysis (6), we included only Caucasian subjects (non-Hispanic; $n = 738$) identified by self-report and confirmed by multidimensional scaling analysis (7).

Genotyping was performed using the Illumina 610-Quad BeadChip using the Tagger algorithm in Haploview (v4.2) (8).

ADNI subjects were scanned with a standardized MRI protocol developed for this cohort (9, 10). High-resolution structural brain MRI scans were acquired at 58 sites using 1.5 T MRI scanners. Additional data collected from a subset of the same subjects, at 3 T, were not analyzed here because of the confounding effects of the different scanner field strength. A sagittal 3D magnetization prepared rapid gradient echo (MP-RAGE) sequence was used, optimized for consistency across sites. repatition time/echo time (TR/TE) = 2,400/1,000 ms; flip angle = 8°; field of view = 24 cm; final reconstructed voxel resolution = 0.9375 × 0.9375 × 1.2 mm^3]. Image corrections were applied using a processing pipeline at the Mayo Clinic as previously described (11, 12). To adjust for global differences in brain positioning and scale, all subjects' scans were linearly registered to the stereotaxic space defined by the International Consortium for Brain Mapping (13) using a nine-parameter transformation (three translations, three rotations, and three scales).

We created a minimal deformation target (MDT) using nonlinear fluid registration with the method proposed by Kochunov et al. (14, 15). An MDT serves as an unbiased average template image to enable automated image registration and reduce statistical bias. Here, an MDT was created from the MRI scans of 40 randomly selected healthy elderly subjects as detailed elsewhere (11, 12).

To quantify 3D patterns of regional volumetric differences throughout the brain, all individual skull-stripped T1-weighted images ($n = 738$) were nonlinearly aligned to a cohort-specific template with an inverse-consistent 3D elastic warping technique using a mutual information cost function (16). For each subject, a separate Jacobian matrix field was derived from the gradients of the deformation field that aligned that individual brain to the MDT template. The determinant of the Jacobian matrix was derived from the deformation field to characterize local volume differences on a voxelwise level.

For this tensor-based morphometry (TBM) analysis, we are carrying forward into another cohort, for validation, the effect of just one single discovered SNP on brain structure, and therefore, there is no need to correct for any more than the one SNP. This practice has been the standard in other work, where the discovery stage is used to pick out a SNP (or a handful of SNPs), and then the multiple testing correction in the second corroborative sample is either not performed or much less heavy, in line with the number of SNPs carried forward (in this case, just one).

Assessing Regional Volume Influences. The TBM assessment of the ADNI cohort suggests cortical volume differences may be driving the connectivity-level association of *SPON1* in the healthy young adults as well. To assess this possibility, we additionally ran TBM on the T1-weighted images of same set of 331 twins processed as for ADNI but controlling for kinship using the mixed model approach. Additionally, the cortical volumes of the posterior cingulate cortex and the superior parietal cortex extracted from FreeSurfer were assessed to determine whether the regional volumes were associated with the connectivity of *SPON1*. Volumes from both hemispheres were analyzed.

Significant associations were seen with respect to localized structural volume in the ADNI cohort in the same regions where we noted altered structural connectivity, and therefore, we set out to determine whether the significant associations of *SPON1* genotype with the posterior cingulate cortex and the superior parietal cortex connection were, in fact, attributable to variation in the volumes of those regions. A TBM analysis of the same 331 twin T1-weighted anatomical images revealed no significant differences in brain volume with respect to rs2618516. Additionally, we extracted the raw volumes for the left and right posterior cingulate cortex and the superior parietal cortex from the FreeSurfer parcellations and found no association to the SNP ($P = 0.748$ for the left posterior cingulate cortex, $P = 0.485$ for the right posterior cingulate cortex, $P = 0.589$ for the left superior parietal cortex, and $P = 0.478$ for the right superior parietal cortex). This null finding suggests that the volume of these regions is not the driving force behind the significant associations found with connectivity.

Cortical Extraction and HARDI Tractography. Nonbrain regions were automatically removed from each T1-weighted MRI scan and a T2-weighted image from the diffusion-weighted image (DWI) set using the FSL tool BET (http://fsl.fmrib.ox.ac.uk/fsl/). A trained neuroanatomical expert manually edited the T1-weighted scans to further refine the brain extraction. Total brain volume estimates were obtained from the manually edited full brain mask to include cerebral, cerebellar, and brainstem regions. All T1-weighted images were linearly aligned using FSL (with 9 degrees of freedom) to a common space (17) with 1-mm isotropic voxels and a 220 × 220 × 220-voxel matrix. Raw diffusion-weighted images were corrected for eddy current distortions using the FSL tool eddy_correct (http://fsl.fmrib.ox.ac.uk/fsl/). For each subject, the 11 eddy-corrected images with no diffusion sensitization were averaged, linearly aligned, and resampled to a downsampled version of their corresponding T1 image (110 × 110 × 110 mm, 2 × 2 × 2 mm). Averaged b_0 maps were elastically registered to the structural scan using a mutual information cost function (16) to compensate for echo planar imaging (EPI)-induced susceptibility artifacts.

The transformation matrix from the linear alignment of the mean b_0 image to the T1-weighted volume was applied to each of 94 gradient directions to properly reorient the orientation distribution functions (ODFs). At each HARDI voxel, ODFs were computed using the normalized and dimensionless ODF estimator derived for *q*-ball imaging in ref. 18. We performed

HARDI tractography on the linearly aligned sets of DWI volumes using these ODFs. Tractography was performed as in ref. 19.

Elastic deformations obtained from the EPI distortion correction, mapping the average b_0 image to the T1-weighted image, were then applied to the tracts 3D coordinates for accurate alignment of the anatomy. Each subject's dataset contained 2,000–10,000 useable fibers (3D curves).

Thirty-five cortical labels per hemisphere, as listed in the Desikan–Killiany atlas (20), were automatically extracted from all aligned T1-weighted structural MRI scans using FreeSurfer (http://surfer.nmr.mgh.harvard.edu/) (21).

Cortical labels extracted are listed.

Region number	Region of interest
1	Banks of the superior temporal sulcus
2	Caudal anterior cingulate
3	Caudal middle frontal
4	Corpus callosum
5	Cuneus
6	Entorhinal
7	Fusiform
8	Inferior parietal
9	Inferior temporal
10	Isthmus of the cingulate
11	Lateral occipital
12	Lateral orbitofrontal
13	Lingual
14	Medial orbitofrontal
15	Middle temporal
16	Parahippocampal
17	Paracentral
18	Pars opercularis
19	Pars orbitalis
20	Pars triangularis
21	Pericalcarine
22	Postcentral
23	Posterior cingulate
24	Precentral
25	Precuneus
26	Rostral anterior cingulate
27	Rostral middle frontal
28	Superior frontal
29	Superior parietal
30	Superior temporal
31	Supramarginal
32	Frontal pole
33	Temporal pole
34	Transverse temporal
35	Insula

The first 35 elements of the matrix (on both the x and y axes) represent the regions on the left hemisphere, whereas numbered labels 36–70 represent the same regions on the right hemisphere.

The resulting T1-weighted images and cortical models were aligned to the original T1-weighted input image space and downsampled using nearest neighbor interpolation to the space of the DWIs (to avoid intermixing of labels). To ensure tracts would intersect cortical labeled boundaries, labels were dilated with an isotropic box kernel of width = 5 voxels as implemented in Matlab (http://www.mathworks.com/).

For each subject, a full 70×70 connectivity matrix was created. Each element described the proportion of the total number of fibers connecting each of the regions; diagonal elements of the matrix describe the total number of fibers passing through a certain cortical region of interest. If more than 5% of subjects had no fibers in a matrix element, then that connection was considered invalid or insufficiently consistent in its occurrence in the population, and it was not included in the analysis.

The flowchart in Fig. S1 shows image processing steps to generate a map of brain fiber connectivity based on an individual's anatomical MRI and diffusion imaging data. To summarize, diffusion-weighted MRI scans are coregistered to a standard anatomical T1-weighted brain image by an image called the average b_0 image. The structural scans undergo automated cortical parcellations, and tractography is performed on the diffusion-weighted MRIs. Cortical labels are uniformly dilated to ensure that they intersect the white matter, where tracts are traced. Tracts are elastically fitted to the labeled structural scan to ensure adequate coregistration. For each subject, a series of colored images is created to overlay the fiber density map, the corresponding T1 image, and the dilated FreeSurfer parcellations. These images were examined to determine which registrations were poor, resulting in subject elimination; 17 subjects were eliminated from this study because of poor coregistration (Fig. S6 shows axial images for a typical subject as well as one subject removed from analysis). Finally, connectivity matrices are created—each matrix element shows the proportion of the total number of detected fibers in the brain that cross or intersect the specific pair of cortical regions at the top and side of the matrix. For all analyses, we control for sex, age, and ICV, which can influence diffusion-based analyses (22) and are associated with connectivity measures (23).

Acknowledgments List for ADNI Publications. The Alzheimer's Disease Neuroimaging Initiative database (www.loni.ucla.edu/ADNI): ADNI data collection was funded by the Alzheimer's Disease Neuroimaging Initiative (ADNI; NIH Grant U01 AG024904). ADNI is funded by the National Institute on Aging, the National Institute of Biomedical Imaging and Bioengineering, Abbott, AstraZeneca AB, Bayer Schering Pharma AG, Bristol-Myers Squibb, Eisai Global Clinical Development, Elan Corporation, Genentech, GE Healthcare, GlaxoSmithKline, Innogenetics, Johnson and Johnson, Eli Lilly and Co., Medpace, Inc., Merck and Co., Inc., Novartis AG, Pfizer Inc, F. Hoffman-La Roche, Schering-Plough, Synarc, Inc., Wyeth, and non-profit partners the Alzheimer's Association and Alzheimer's Drug Discovery Foundation, with participation from the U.S. Food and Drug Administration. Private sector contributions to ADNI are facilitated by the Foundation for the National Institutes of Health (www.fnih.org) The grantee organization is the Northern California Institute for Research and Education, and the study is coordinated by the Alzheimer's Disease Cooperative Study at the University of California, San Diego. ADNI data are disseminated by the Laboratory of Neuro Imaging at the University of California, Los Angeles. The Data and Publications Committee, in keeping with the publication policies adopted by the ADNI Steering Committee, here provided lists for standardized acknowledgment. The list consists of two parts: Infrastructure Investigators and Site Investigators. Infrastructure Investigators represent the names responsible for leadership and infrastructure. Site Investigators represent the names of individuals at each recruiting site. All papers, including methodological papers, should have an acknowledgment list that consists of Infrastructure Investigators plus the full list.

Part A: Leadership and Infrastructure

- Principal Investigator :
  - Michael Weiner, MD UC San Francisco
- ADCS PI and Director of Coordinating Center Clinical Core:
  - Paul Aisen, MD UC San Diego
- Executive Committee:
  - Michael Weiner, MD UC San Francisco
  - Paul Aisen, MD UC San Diego

- Ronald Petersen, MD, PhD Mayo Clinic, Rochester
- Clifford R. Jack, Jr., MD Mayo Clinic, Rochester
- William Jagust, MD UC Berkeley
- John Q. Trojanowski, MD, PhD U Pennsylvania
- Arthur W. Toga, PhD UCLA
- Laurel Beckett, PhD UC Davis
- Robert C. Green, MD, MPH Brigham and Women's Hospital/Harvard Medical School
- Andrew J. Saykin, PsyD Indiana University
- John Morris, MD Washington University St. Louis

- ADNI 2 Private Partner Scientific Board (PPSB) Chair
  - Enchi Liu, PhD Janssen Alzheimer Immunotherapy

- Data and Publication Committee (DPC)
  - Robert C. Green, MD, MPH Brigham and Women's Hospital/Harvard Medical School (Chair)

- Resource Allocation Review Committee
  - Tom Montine, MD, PhD University of Washington (Chair)

- Clinical Core Leaders
  - Ronald Petersen, MD, PhD Mayo Clinic, Rochester (Core PI)
  - Paul Aisen, MD UC San Diego

- Clinical Informatics and Operations
  - Anthony Gamst, PhD UC San Diego
  - Ronald G. Thomas, PhD UC San Diego
  - Michael Donohue, PhD UC San Diego
  - Sarah Walter, MSc UC San Diego
  - Devon Gessert UC San Diego
  - Tamie Sather UC San Diego

- Biostatistics Core Leaders and Key Personnel
  - Laurel Beckett, PhD UC Davis (Core PI)
  - Danielle Harvey, PhD UC Davis
  - Anthony Gamst, PhD UC San Diego
  - Michael Donohue, PhD UC San Diego
  - John Kornak, PhD UC Davis

- MRI Core Leaders and Key Personnel
  - Clifford R. Jack, Jr., MD Mayo Clinic, Rochester (Core PI)
  - Anders Dale, PhD UC San Diego
  - Matthew Bernstein, PhD Mayo Clinic, Rochester
  - Joel Felmlee, PhD Mayo Clinic, Rochester
  - Nick Fox, MD University of London
  - Paul Thompson, PhD UCLA School of Medicine
  - Norbert Schuff, PhD UCSF MRI
  - Gene Alexander, PhD Banner Alzheimer's Institute
  - Charles DeCarli, MD UC Davis

- PET Core Leaders and Key Personnel
  - William Jagust, MD UC Berkeley (Core PI)
  - Dan Bandy, MS, CNMT Banner Alzheimer's Institute
  - Robert A. Koeppe, PhD University of Michigan
  - Norm Foster, MD University of Utah
  - Eric M. Reiman, MD Banner Alzheimer's Institute
  - Kewei Chen, PhD Banner Alzheimer's Institute
  - Chet Mathis, MD University of Pittsburgh

- Neuropathology Core Leaders
  - John Morris, MD Washington University St. Louis
  - Nigel J. Cairns, PhD, MRCPath Washington University St. Louis
  - Lisa Taylor-Reinwald, BA, HTL Washington University St. Louis

- Biomarkers Core Leaders and Key Personnel
  - J.Q. Trojanowki, MD, PhD UPenn School of Medicine (Core PI)
  - Les Shaw, PhD UPenn School of Medicine
  - Virginia M.Y. Lee, PhD, MBA UPenn School of Medicine
  - Magdalena Korecka, PhD UPenn School of Medicine

- Informatics Core Leaders and Key Personnel
  - Arthur W. Toga, PhD UCLA (Core PI)
  - Karen Crawford UCLA
  - Scott Neu, PhD UCLA

- Genetics Core Leaders and Key Personnel
  - Andrew J. Saykin, PsyD Indiana University
  - Tatiana M. Foroud, PhD Indiana University
  - Steven Potkin, MD UC Irvine
  - Li Shen, PhD Indiana University

- Early Project Development
  - Zaven Khachaturian, PhD Khachaturian, Radebaugh & Associates (KRA), Inc
  - Alzheimer's Association's Ronald and Nancy Reagan's Research Institute
  - Richard Frank, MD, PhD General Electric
  - Peter J. Snyder, PhD University of Connecticut
  - NIA
  - Susan Molchan, PhD National Institute on Aging/National Institutes of Health

Part B: Investigators By Site

- FULL ADNI Investigator Lists:
  - Oregon Health and Science University:
    - Jeffrey Kaye, MD
    - Joseph Quinn, MD
    - Betty Lind, BS
    - Sara Dolen, BS – Past Investigator
  - University of Southern California:
    - Lon S. Schneider, MD
    - Sonia Pawluczyk, MD
    - Bryan M. Spann, DO, PhD
  - University of California–San Diego:
    - James Brewer, MD, PhD
    - Helen Vanderswag, RN
  - University of Michigan:
    - Judith L. Heidebrink, MD, MS
    - Joanne L. Lord, LPN, BA, CCRC
  - Mayo Clinic, Rochester:
    - Ronald Petersen, MD, PhD
    - Kris Johnson, RN
  - Baylor College of Medicine:
    - Rachelle S. Doody, MD, PhD
    - Javier Villanueva-Meyer, MD
    - Munir Chowdhury, MBBS, MS
  - Columbia University Medical Center:
    - Yaakov Stern, PhD
    - Lawrence S. Honig, MD, PhD
    - Karen L. Bell, MD
  - Washington University, St. Louis:
    - John C. Morris, MD
    - Beau Ances, MD
    - Maria Carroll, RN, MSN

- Sue Leon, RN, MSN
- Mark A. Mintun, MD – Past Investigator
- Stacy Schneider, APRN, BC, GNP – Past Investigator

○ University of Alabama - Birmingham:
- Daniel Marson, JD, PhD
- Randall Griffith, PhD, ABPP
- David Clark, MD

○ Mount Sinai School of Medicine:
- Hillel Grossman, MD
- Effie Mitsis, PhD
- Aliza Romirowsky, BA

○ Rush University Medical Center:
- Leyla deToledo-Morrell, PhD
- Raj C. Shah, MD

○ Wein Center:
- Ranjan Duara, MD
- Daniel Varon, MD
- Peggy Roberts, CNA

○ Johns Hopkins University:
- Marilyn Albert, PhD
- Chiadi Onyike, MD, MHS
- Stephanie Kielb, MD

○ New York University:
- Henry Rusinek, PhD
- Mony J de Leon, EdD
- Lidia Glodzik, MD, PhD
- Susan De Santi, PhD – Past Investigator

○ Duke University Medical Center:
- P. Murali Doraiswamy, MD
- Jeffrey R. Petrella, MD
- R. Edward Coleman, MD

○ University of Pennsylvania:
- Steven E. Arnold, MD
- Jason H. Karlawish, MD
- David Wolk, MD

○ University of Kentucky:
- Charles D. Smith, MD
- Greg Jicha, MD
- Peter Hardy, PhD

○ University of Pittsburgh:
- Oscar L. Lopez, MD
- MaryAnn Oakley, MA
- Donna M. Simpson, CRNP, MPH

○ University of Rochester Medical Center:
- Anton P. Porsteinsson, MD
- Bonnie S. Goldstein, MS, NP
- Kim Martin, RN
- Kelly M. Makino, BS – Past Investigator
- M. Saleem Ismail, MD – Past Investigator
- Connie Brand, RN – Past Investigator

○ University of California, Irvine:
- Ruth A. Mulnard, DNSc, RN, FAAN
- Gaby Thai, MD
- Catherine Mc-Adams-Ortiz, MSN, RN, A/GNP

○ University of Texas Southwestern Medical School:
- Kyle Womack, MD
- Dana Mathews, MD, PhD
- Mary Quiceno, MD
- Ramon Diaz-Arrastia, MD, PhD – Past Investigator
- Richard King, MD – Past Investigator
- Myron Weiner, MD – Past Investigator
- Kristen Martin-Cook, MA – Past Investigator
- Michael DeVous, PhD – Past Investigator

○ Emory University:
- Allan I. Levey, MD, PhD
- James J. Lah, MD, PhD
- Janet S. Cellar, DNP, PMHCNS-BC

○ University of Kansas, Medical Center:
- Jeffrey M. Burns, MD
- Heather S. Anderson, MD
- Russell H. Swerdlow, MD

○ University of California, Los Angeles:
- Liana Apostolova, MD
- Po H. Lu, PsyD
- George Bartzokis, MD – Past Investigator
- Daniel H.S. Silverman, MD, PhD – Past Investigator

○ Mayo Clinic, Jacksonville:
- Neill R Graff-Radford, MBBCH, FRCP (London)
- Francine Parfitt, MSH, CCRC
- Heather Johnson, MLS, CCRP

○ Indiana University:
- Martin R. Farlow, MD
- Ann Marie Hake, MD
- Brandy R. Matthews, MD
- Scott Herring, RN – Past Investigator

○ Yale University School of Medicine:
- Christopher H. van Dyck, MD
- Richard E. Carson, PhD
- Martha G. MacAvoy, PhD

○ McGill Univ., Montreal-Jewish General Hospital:
- Howard Chertkow, MD
- Howard Bergman, MD
- Chris Hosein, MEd

○ Sunnybrook Health Sciences, Ontario:
- Sandra Black, MD, FRCPC
- Dr Bojana Stefanovic
- Curtis Caldwell, PhD

○ U.B.C. Clinic for AD & Related Disorders:
- Ging-Yuek Robin Hsiung, MD, MHSc, FRCPC
- Howard Feldman, MD, FRCPC
- Benita Mudge, BS
- Michele Assaly, MA – Past Investigator

○ Cognitive Neurology - St. Joseph's, Ontario:
- Andrew Kertesz, MD
- John Rogers, MD
- Dick Trost, PhD

○ Cleveland Clinic Lou Ruvo Center for Brain Health:
- Charles Bernick, MD
- Donna Munic, PhD

- Northwestern University:
  - Diana Kerwin, MD
  - Marek-Marsel Mesulam, MD
  - Kristina Lipowski, BA
  - Chuang-Kuo Wu, MD, PhD – Past Investigator
  - Nancy Johnson, PhD – Past Investigator

- Premiere Research Inst (Palm Beach Neurology):
  - Carl Sadowsky, MD
  - Walter Martinez, MD
  - Teresa Villena, MD

- Georgetown University Medical Center:
  - Raymond Scott Turner, MD, PhD
  - Kathleen Johnson, NP
  - Brigid Reynolds, NP

- Brigham and Women's Hospital:
  - Reisa A. Sperling, MD
  - Keith A. Johnson, MD
  - Gad Marshall, MD
  - Meghan Frey – Past Investigator

- Stanford University:
  - Jerome Yesavage, MD
  - Joy L. Taylor, PhD
  - Barton Lane, MD
  - Allyson Rosen, PhD – Past Investigator
  - Jared Tinklenberg, MD – Past Investigator

- Banner Sun Health Research Institute:
  - Marwan Sabbagh, MD, FAAN, CCRI
  - Christine Belden, PsyD
  - Sandra Jacobson, MD

- Boston University:
  - Neil Kowall, MD
  - Ronald Killiany, PhD
  - Andrew E. Budson, MD
  - Alexander Norbash, MD – Past Investigator
  - Patricia Lynn Johnson, BA – Past Investigator

- Howard University:
  - Thomas O. Obisesan, MD, MPH
  - Saba Wolday, MSc
  - Salome K. Bwayo, PharmD – Past Investigator

- Case Western Reserve University:
  - Alan Lerner, MD
  - Leon Hudson, MPH
  - Paula Ogrocki, PhD

- University of California, Davis – Sacramento:
  - Evan Fletcher, PhD
  - Owen Carmichael, PhD
  - John Olichney, MD
  - Charles DeCarli, MD – Past Investigator

- Neurological Care of CNY:
  - Smita Kittur, MD

- Parkwood Hospital:
  - Michael Borrie, MB ChB
  - T-Y Lee, PhD
  - Dr Rob Bartha, PhD

- University of Wisconsin:
  - Sterling Johnson, PhD
  - Sanjay Asthana, MD
  - Cynthia M. Carlsson, MD

- University of California, Irvine - BIC:
  - Steven G. Potkin, MD
  - Adrian Preda, MD
  - Dana Nguyen, PhD

- Banner Alzheimer's Institute:
  - Pierre Tariot, MD
  - Adam Fleisher, MD
  - Stephanie Reeder, BA

- Dent Neurologic Institute:
  - Vernice Bates, MD
  - Horacio Capote, MD
  - Michelle Rainka, PharmD, CCRP

- Ohio State University:
  - Douglas W. Scharre, MD
  - Maria Kataki, MD, PhD

- Albany Medical College:
  - Earl A. Zimmerman, MD
  - Dzintra Celmins, MD
  - Alice D. Brown, FNP – Past Investigator

- Hartford Hosp, Olin Neuropsychiatry Research Center:
  - Godfrey D. Pearlson, MD
  - Karen Blank, MD
  - Karen Anderson, RN

- Dartmouth-Hitchcock Medical Center:
  - Andrew J. Saykin, PsyD
  - Robert B. Santulli, MD
  - Eben S. Schwartz, PhD

- Wake Forest University Health Sciences:
  - Kaycee M. Sink, MD, MAS
  - Jeff D. Williamson, MD, MHS
  - Pradeep Garg, PhD
  - Franklin Watkins, MD – Past Investigator

- Rhode Island Hospital:
  - Brian R. Ott, MD
  - Henry Querfurth, MD
  - Geoffrey Tremont, PhD

- Butler Hospital:
  - Stephen Salloway, MD, MS
  - Paul Malloy, PhD
  - Stephen Correia, PhD

- UC San Francisco:
  - Howard J. Rosen, MD
  - Bruce L. Miller, MD

- Medical University South Carolina:
  - Jacobo Mintzer, MD, MBA
  - Crystal Flynn Longmire, PhD
  - Kenneth Spicer, MD, PhD

- St. Joseph's Health Care:
  - Elizabeth Finger, MD
  - Irina Rachinsky, MD
  - John Rogers, MD
  - Andrew Kertesz, MD – Past Investigator
  - Dick Drost, MD – Past Investigator

1. Annett M (1970) A classification of hand preference by association analysis. *Br J Psychol* 61(3):303–321.
2. Medland SE, et al. (2009) Common variants in the trichohyalin gene are associated with straight hair in Europeans. *Am J Hum Genet* 85(5):750–755.
3. Abecasis GR, Cherny SS, Cookson WO, Cardon LR (2001) GRR: Graphical representation of relationship errors. *Bioinformatics* 17(8):742–743.
4. Jones DK, Horsfield MA, Simmons A (1999) Optimal strategies for measuring diffusion in anisotropic systems by magnetic resonance imaging. *Magn Reson Med* 42(3): 515–525.
5. Boker S, et al. (2011) OpenMx: An open source extended structural equation modeling framework. *Psychometrika* 76(2):306–317.
6. Lander ES, Schork NJ (1994) Genetic dissection of complex traits. *Science* 265(5181): 2037–2048.
7. Stein JL, et al. (2010) Genome-wide analysis reveals novel genes influencing temporal lobe structure with relevance to neurodegeneration in Alzheimer's disease. *Neuroimage* 51(2):542–554.
8. Barrett JC, Fry B, Maller J, Daly MJ (2005) Haploview: Analysis and visualization of LD and haplotype maps. *Bioinformatics* 21(2):263–265.
9. Leow AD, et al. (2006) Longitudinal stability of MRI for mapping brain change using tensor-based morphometry. *Neuroimage* 31(2):627–640.
10. Jack CR, Jr., et al. (2008) The Alzheimer's Disease Neuroimaging Initiative (ADNI): MRI methods. *J Magn Reson Imaging* 27(4):685–691.
11. Hua X, et al. (2008) 3D characterization of brain atrophy in Alzheimer's disease and mild cognitive impairment using tensor-based morphometry. *Neuroimage* 41(1): 19–34.
12. Hua X, et al. (2008) Tensor-based morphometry as a neuroimaging biomarker for Alzheimer's disease: An MRI study of 676 AD, MCI, and normal subjects. *Neuroimage* 43(3):458–469.
13. Mazziotta J, et al. (2001) A four-dimensional probabilistic atlas of the human brain. *J Am Med Inform Assoc* 8(5):401–430.
14. Kochunov P, et al. (2001) Regional spatial normalization: Toward an optimal target. *J Comput Assist Tomogr* 25(5):805–816.
15. Kochunov P, et al. (2002) An optimized individual target brain in the Talairach coordinate system. *Neuroimage* 17(2):922–927.
16. Leow A, et al. (2005) Inverse consistent mapping in 3D deformable image registration: Its construction and statistical properties. *Inf Process Med Imaging* 19:493–503.
17. Holmes CJ, et al. (1998) Enhancement of MR images using registration for signal averaging. *J Comput Assist Tomogr* 22(2):324–333.
18. Aganj I, et al. (2010) Reconstruction of the orientation distribution function in single- and multiple-shell q-ball imaging within constant solid angle. *Magn Reson Med* 64(2):554–566.
19. Aganj I, et al. (2011) A Hough transform global probabilistic approach to multiple-subject diffusion MRI tractography. *Med Image Anal* 15(4):414–425.
20. Desikan RS, et al. (2006) An automated labeling system for subdividing the human cerebral cortex on MRI scans into gyral based regions of interest. *Neuroimage* 31(3):968–980.
21. Fischl B, et al. (2004) Automatically parcellating the human cerebral cortex. *Cereb Cortex* 14(1):11–22.
22. Takao H, Hayashi N, Inano S, Ohtomo K (2011) Effect of head size on diffusion tensor imaging. *Neuroimage* 57(3):958–967.
23. Yan C, et al. (2011) Sex- and brain size-related small-world structural cortical networks in young adults: A DTI tractography study. *Cereb Cortex* 21(2):449–458.

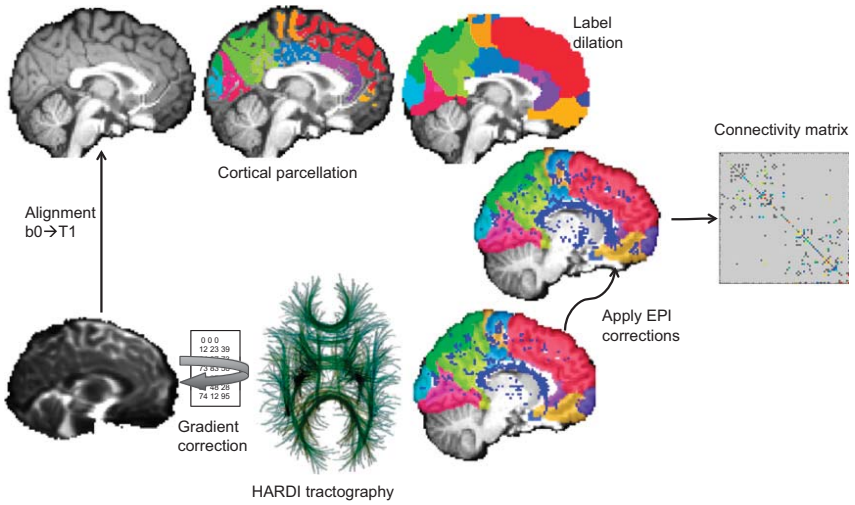

Fig. S1. A flowchart shows image processing steps to generate a map of brain fiber connectivity based on an individual's MRI and diffusion imaging data. As detailed in *Materials and Methods*, diffusion-weighted MRI scans are coregistered to a standard anatomical T1-weighted brain image by an image called the average b_0 image. The structural scans undergo automated cortical parcellations, and tractography is performed on the diffusion-weighted MRIs. Cortical labels are uniformly dilated to ensure that they intersect the white matter, where tracts are traced. Tracts are elastically fitted to the labeled structural scan to ensure adequate coregistration. Connectivity matrices are created—each element in the matrix shows the proportion of the total number of detected fibers in the brain that crosses or intersects the specific pair of cortical regions at the top and side of the matrix.

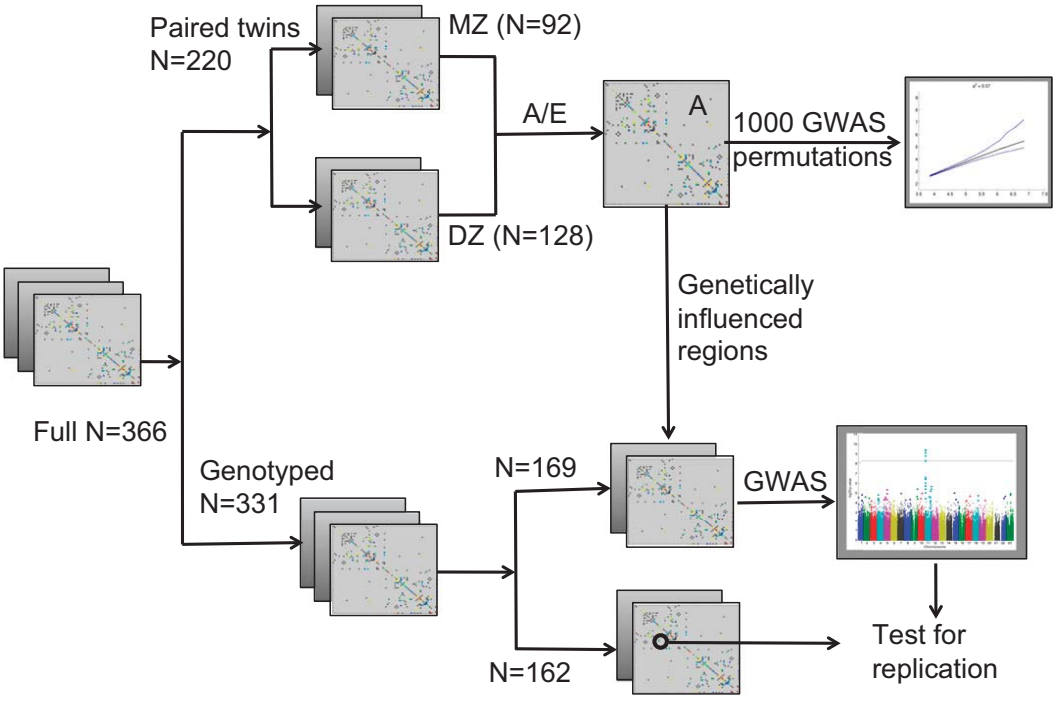

Fig. S2. The pipeline for screening brain connectivity maps for effects of single-letter differences in the genetic code. After network connectivity matrices were created from the MRI and HARDI brain scans, 220 pairs of twins were separated into MZs and DZs to estimate heritability through structural equation modeling. The A/E model gave the best fit to the overall matrix, and it accounts for additive genetic effects (A) and unique environmental effects (E) of the group. Regions where at least 1% of the variance was attributable to additive genetic factors were carried forward for additional analysis; 1,000 permutations of the connection value (fiber proportion between connections) were conducted while preserving family structure and including age, sex, and ICVs as covariates, and 331 genotyped individuals were split by study identification numbers into two roughly equal groups of distinct families. The slightly larger group was used as a discovery sample. When a significant locus was found, it was further replicated in the second independent sample of the data, which had been deliberately excluded from the initial analysis.

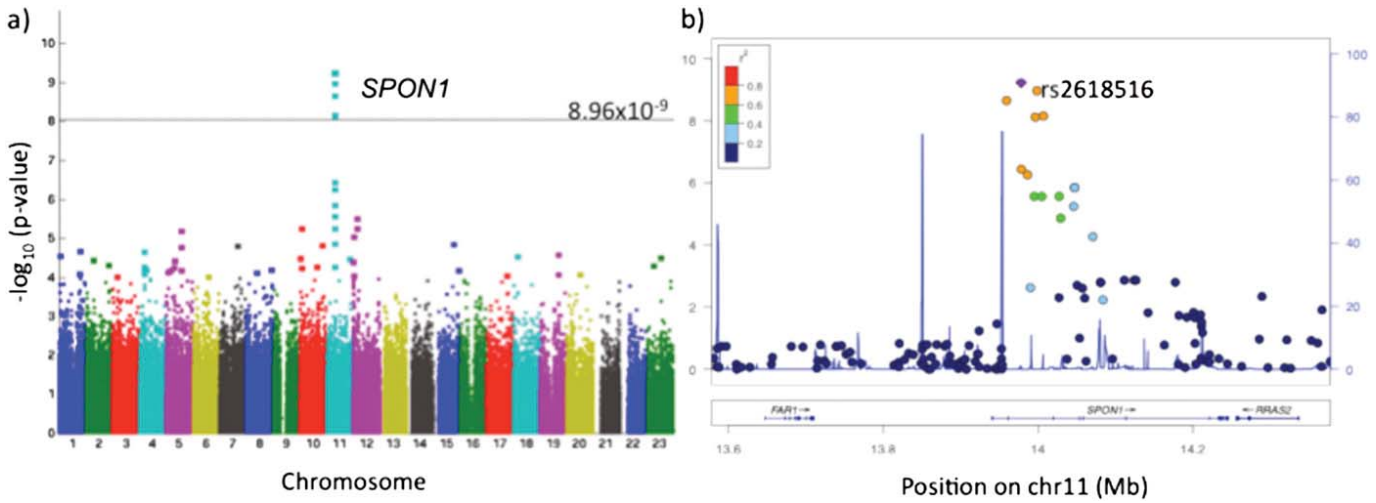

Fig. S3. Genome-wide association analysis of the full twin sample ($n = 331$), at every connection, leads to a single SNP reaching genome-wide significance ($P < 8.96 \times 10^{-9}$) for one network connection. (*A*) The Manhattan plot is shown for the connection between the left superior parietal cortex and the left posterior cingulate, where variants in *SPON1* were found to be significant after this extremely conservative correction. (*B*) The locus is displayed focusing in on the region using LocusZoom (https://statgen.sph.umich.edu/locuszoom/).

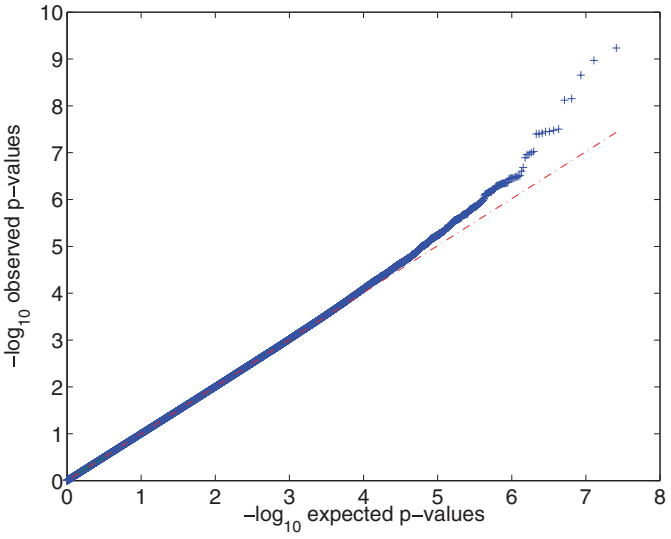

Fig. S4. A quantile–quantile plot shows the connectome-wide, genome-wide result. All *P* values from all 59 genome-wide associations were combined to show the observed distribution of *P* values with respect to those *P* values expected from a normal distribution.

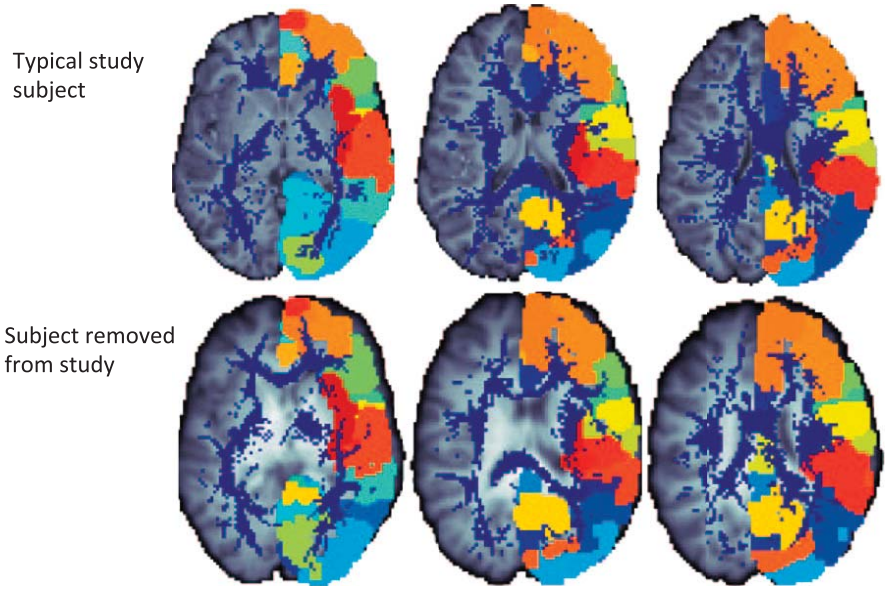

Fig. S5. For each subject, a series of colored images is created to overlay the fiber density map, the corresponding T1-weighted image, and the dilated FreeSurfer parcellations. Examination of these images allowed us to determine which registrations were poor, resulting in subject elimination. Axial images are shown for a typical subject (*Upper*) as well as one of those subjects removed from analysis because of poor alignment and high levels of EPI distortions (*Lower*).

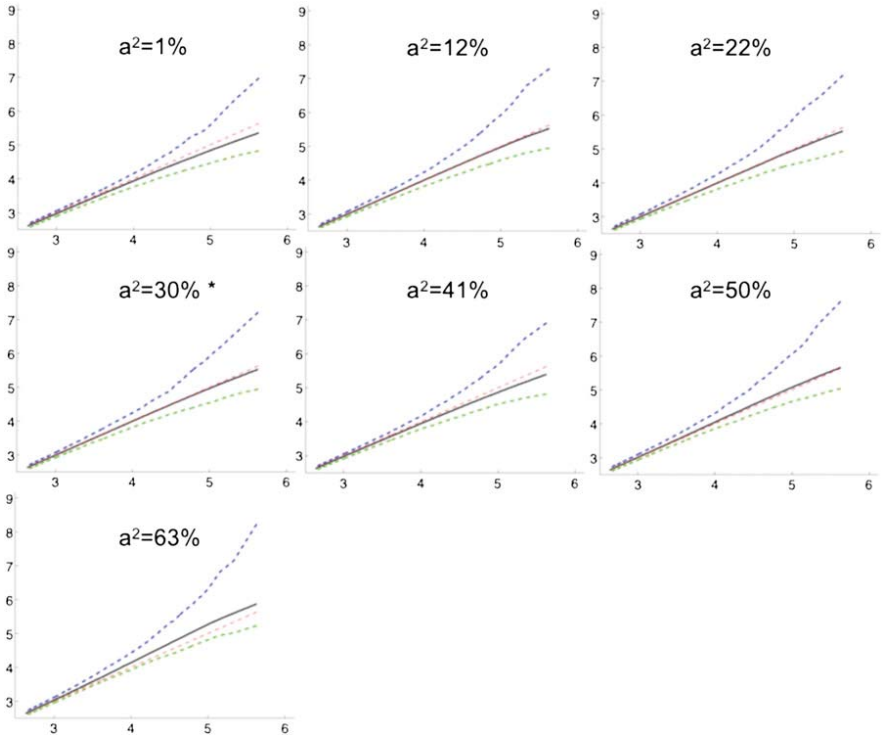

Fig. S6. One thousand GWASs were conducted on permutations of the twin connectivity matrices used for the A/C/E heritability analysis. The point of these plots is to show that the analyses do not yield findings by chance when the genomic scan is carried out on randomized data. The $-\log_{10}$ of the lowest 1,000 *P* values of each permutation is shown plotted against the $-\log_{10}$ expected ordered *P* values for the same number of tests. The solid black line represents the mean of the ordered *P* values, whereas the dashed blue and green lines represent the 0.025 and 0.975 pointwise quantiles of the ordered *P* values, respectively. The dashed red line represents the expected null distribution of *P* values. Regardless of heritability of the node, genome-wide associations of permuted values do not deviate from the expected null distribution. *Permutations at the node where the genome-wide significant discovery was made.

Table S1. The additive genetic component of the variance estimated from the model and the 95% confidence intervals (CIs) for all connections examined

From	To	a^2 (Heritability)	95% CI
Caudal middle frontal-L	Caudal middle frontal-L	0.01	>0, 0.28
Superior frontal-L	Rostral middle frontal-L	0.05	>0, 0.31
Superior frontal-L	Medial orbitofrontal-L	0.13	>0, 0.36
Superior parietal-R	Lateral occipital-R	0.13	>0, 0.38
Lateral occipital-R	Inferior temporal-R	0.13	>0, 0.4
Superior frontal-R	Rostral middle frontal-R	0.13	>0, 0.36
Insula-R	Pars opercularis-R	0.14	>0, 0.39
Insula-L	Postcentral-L	0.17	>0, 0.43
Pars opercularis-R	Pars opercularis-R	0.17	>0, 0.44
Precentral-L	Postcentral-L	0.20	>0, 0.43
Medial orbitofrontal-L	Medial orbitofrontal-L	0.22	>0, 0.46
Medial orbitofrontal-R	Medial orbitofrontal-R	0.22	>0, 0.44
Lateral occipital-R	Fusiform-R	0.22	>0, 0.47
Superior frontal-R	Superior frontal-R	0.24	0.02, 0.45
Precuneus-R	Lateral occipital-R	0.26	>0, 0.51
Lateral orbitofrontal-R	Lateral orbitofrontal-R	0.27	>0, 0.52
Superior parietal-R	Precuneus-R	0.27	>0, 0.52
Precentral-L	Posterior cingulate-L	0.27	0.03, 0.5
Precentral-R	Paracentral-R	0.29	0.06, 0.51
Superior parietal-L	Posterior cingulate-L	0.30	0.04, 0.54
Insula-L	Precentral-L	0.31	0.06, 0.53
Rostral middle frontal-R	Caudal middle frontal-R	0.32	0.07, 0.55
Pericalcarine-R	Lateral occipital-R	0.34	0.11, 0.55
Lingual-R	Lingual-R	0.34	0.07, 0.6
Insula-L	Insula-L	0.35	0.13, 0.56
Fusiform-R	Fusiform-R	0.35	0.11, 0.57
Rostral anterior cingulate-L	Lateral orbitofrontal-L	0.36	0.1, 0.59
Precuneus-R	Precuneus-R	0.36	0.1, 0.59
Pericalcarine-L	Lateral occipital-L	0.36	0.13, 0.58
Superior frontal-L	Paracentral-L	0.36	0.14, 0.56
Paracentral-L	Paracentral-L	0.37	0.13, 0.58
Superior parietal-R	Superior parietal-R	0.37	0.14, 0.58
Lateral occipital-L	Lateral occipital-L	0.38	0.13, 0.6
Precentral-L	Paracentral-L	0.38	0.17, 0.58
Cuneus-L	Cuneus-L	0.39	0.18, 0.58
Fusiform-L	Fusiform-L	0.39	0.17, 0.59
Precuneus-L	Isthmus of the cingulate-L	0.40	0.18, 0.59
Pars opercularis-L	Pars opercularis-L	0.41	0.18, 0.61
Rostral middle frontal-L	Rostral middle frontal-L	0.41	0.17, 0.62
Precentral-L	Precentral-L	0.42	0.2, 0.61
Posterior cingulate-R	Paracentral-R	0.42	0.17, 0.63
Medial orbitofrontal-R	Lateral orbitofrontal-R	0.43	0.19, 0.64
Precuneus-R	Posterior cingulate-R	0.44	0.17, 0.66
Precuneus-L	Lateral occipital-L	0.44	0.21, 0.64
Inferior temporal-R	Inferior temporal-R	0.45	0.22, 0.64
Superior parietal-L	Superior parietal-L	0.47	0.26, 0.65
Posterior cingulate-L	Paracentral-L	0.47	0.24, 0.66
Supramarginal-R	Postcentral-R	0.47	0.26, 0.66
Inferior temporal-R	Fusiform-R	0.48	0.26, 0.66
Postcentral-R	Postcentral-R	0.49	0.24, 0.68
Precuneus-R	Precuneus-L	0.50	0.26, 0.69
Insula-R	Fusiform-R	0.50	0.26, 0.69
Caudal middle frontal-R	Caudal middle frontal-R	0.57	0.36, 0.73
Insula-R	Insula-R	0.58	0.39, 0.73
Posterior cingulate-L	Posterior cingulate-L	0.63	0.44, 0.77
Insula-R	Supramarginal-R	0.64	0.46, 0.77
Precentral-R	Precentral-R	0.66	0.48, 0.79
Precuneus-L	Posterior cingulate-L	0.66	0.49, 0.79
Precuneus-L	Precuneus-L	0.67	0.49, 0.8

Table S2. Genome-wide significant associations are detected at a single locus in the *SPON1* gene when examining the genetic variability associated with fiber proportions connecting cortical regions in 331 subjects

Connection	Gene	SNP	MAF	*P* value	*B* value
L-superior parietal and L-posterior cingulate	SPON1	rs2697846	0.38 (T)	2.22×10^{-9}	0.0018
L-superior parietal and L-posterior cingulate	SPON1	rs2618516	0.36 (T)	5.82×10^{-10}	0.0018
L-superior parietal and L-posterior cingulate	SPON1	rs10832160	0.34(G)	7.58×10^{-9}	0.0017
L-superior parietal and L-posterior cingulate	SPON1	rs11023052	0.34 (T)	1.07×10^{-9}	0.0018
L-superior parietal and L-posterior cingulate	SPON1	rs7124311	0.33 (G)	7.02×10^{-9}	0.0017

SPON1 was initially discovered and replicated in samples of one-half this size ($N_{discovery} = 169$; $N_{replication} = 162$). Even with a stringent classical Bonferroni correction over all tests ($0.05/59 \times 428{,}287 = 1.98 \times 10^{-9}$), two SNPs would still have survived significance. *B* values represent the unstandardized regression coefficient; here, the minor allele is associated with increased fiber connectivity. MAF, minor allele frequency.

Table S3. The 15 most significant SNPs (with lowest *P* values) found for all topological network measures are listed

SNP	Gene within 50 kB	Chromosome	*P* value	Topological measure	Node/global
rs16997087	*MACROD2*	20	1.11E-10	Strength	R paracentral
rs17819300	*NEDD4*	15	1.36E-10	Strength	R-banks of the superior temporal sulcus
rs7879933	*UBE2A*	X	1.83E-10	Strength	R-inferior parietal
rs17819282	*NEDD4*	15	2.78E-10	Strength	R-banks of the superior temporal sulcus
rs17238489	*NEDD4*	15	4.45E-10	Strength	R-banks of the superior temporal sulcus
rs2175104	*NEDD4*	15	7.84E-10	Strength	R-banks of the superior temporal sulcus
rs4747011	*LRRC20*	10	9.27E-10	Strength	L-transverse temporal
rs2224003	—	6	9.82E-10	Strength	R-*pars opercularis*
rs17024684	*CNTN4*	3	1.99E-09	Clustering coefficient	L-isthmus of the cingulate
rs16997087	*MACROD2*	20	2.30E-09	Efficiency	R-paracentral
rs9834692	—	3	3.01E-09	Clustering coefficient	R-insula
rs9883474	—	3	3.01E-09	Clustering coefficient	R-insula
rs3771863	*TACR1*	2	3.47E-09	Strength	L-inferior parietal
rs10485022	—	6	4.76E-09	Strength	R-*pars opercularis*
rs7629924	*CNTN4*	3	4.76E-09	Clustering coefficient	L-isthmus of the cingulate

Here, local measures of network strength yielded genome-wide significant findings at the strict significance threshold set (described in *Materials and Methods*). These SNPs include rs16997087 near the *MACROD2* gene ($P = 1.11 \times 10^{-10}$), rs17819300 and rs17819282 in linkage disequilibrium inside the *NEDD4* gene ($P = 1.36 \times 10^{-10}$ and $P = 2.78 \times 10^{-10}$), and rs7879933 in the *UCE2A* gene ($P = 1.83 \times 10^{-10}$) of the X chromosome. Local measures of clustering coefficient and efficiency provided suggestive associations (defined here as $5 \times 10^{-8} < P < 3.39 \times 10^{-10}$), where 5×10^{-8} is the classical threshold for a single GWAS with this density of SNPs and 3.39×10^{-10} is the genome-wide significance threshold corrected for the number of tests. We found no suggestive genome-wide significant variants for Eigenvector centrality or any of the global measures, because the lowest *P* value in all cases was $>5 \times 10^{-8}$.